Automated Multiprobe Microassembly Using Vision Feedback

John D. Wason, *Member, IEEE*, John T. Wen, *Fellow, IEEE*, Jason J. Gorman, and Nicholas G. Dagalakis, *Life Senior Member, IEEE*

***Abstract*—This paper describes the algorithm development and experimental results of a vision-guided multiprobe microassembly system. The key focus is to develop the capabilities required for the construction of 3-D structures using only planar microfabricated parts. Instead of using grippers, multiple sharp-tipped probes are coordinated to manipulate parts by using vision feedback. This novel probe-based approach offers both stable part grasping and dexterous part manipulation. The light weight of the part and relatively slow motion means that only kinematics-based control is required. However, probe motions need to be carefully coordinated to ensure reliable and repeatable part grasping and manipulation. Machine vision with multiple cameras is used to guide the motion. No contact force sensor is used; instead, vision sensing of the probe bending is used for the grasp force control. By combining preplanned manipulation sequences and vision-based manipulation, repeatable spatial (in contrast with planar) manipulation and insertion of a submillimeter part have been demonstrated with an experimental testbed consisting of two actuated probes, a passive probe, an actuated die stage, and two cameras for vision feedback.**

***Index Terms*—Computer vision, dexterous manipulation, force and tactile sensing, grasping, micro/nano robots.**

I. Introduction

MICROASSEMBLY research arose from optoelectronics packaging needs (placement, alignment, and bonding of heterogeneous parts) in the communication industry [1]. The field has since broadened to address the construction of complex microscale structures from heterogeneous basic blocks. Microassembly has the potential to overcome some inherent limits of monolithic bulk micromachined microelectromechanical system (MEMS) devices [2]–[4]. Standard micromachining processes work well on planar devices, but it is difficult to fabricate complex spatial mechanisms. The ability to layer mechanical components is limited by the underlying photolithography approach. It is also hampered by the difficulty in fabrication using different types of materials. The wafer material is homogeneous at the start of the MEMS fabrication process, and different materials can only be deposited in layers on the same wafer substrate. Microassembly can be used to overcome these limitations by assembling components fabricated with different micromachining processes that would otherwise be incompatible.

Microassembly technology may be divided into two general categories: the assembly of discrete components on a larger wafer, such as attaching photonics components to a microchip [5]–[8], or the assembly of a microstruture, such as a microrobot or multipart optical device from discrete components [9]–[13]. The design requirements are quite different—the discrete placement task often favors speed over accuracy and does not require 3-D dexterity over the orientation of the part, while a multipart robot or structure will require very tight tolerances and high spatial dexterity with speed being a secondary requirement.

Previous work on microassembly has primarily focused on the use of microgrippers. The grippers may be based on bimorph metals, piezoelectric ceramics [14], or are silicon MEMS devices themselves [15]–[19]. The use of microgrippers is attractive, as conventional macroscale robot task and path planning techniques may be applied. However, adhesion forces, consisting of electrostatic attraction, van der Waals force, and capillary forces [20], tend to dominate in the microscale. As a result, parts may stick to the gripper even after opening, which then requires additional mechanism or manipulation to overcome (such as the three-prong microgripper in [21]). These grippers can also be brittle and easily damaged. To avoid these problems, parts may have specialized grip points [22], [23] or have built-in "snap" connectors [1], [17]. Multi-degree-of-freedom (DOF) macroscale robotic mechanisms are typically needed to provide dexterous control of the microgripper [16]. This adds to the complexity, size, and is a potential source of disturbance to the microassembly system.

Our research is motivated by the following inquiry: *Can two probes be used more effectively than a conventional two-tine microgripper?* This paper provides a partial answer—the multiprobe micromanipulation approach is at least a viable alternative, particularly for parts with a wide range of scales and geometries. The problem addressed in this paper is to simply reorient a small (submillimeter) planar part and insert it vertically into a slot. The part needs to be lifted, rotated out of plane, aligned, and inserted. Fig. 1 shows a photo of the part before it is picked up and after it has been inserted. This simple task

Manuscript received November 10, 2011; revised April 9, 2012; accepted May 8, 2012. Date of publication June 13, 2012; date of current version September 28, 2012. This paper was recommended for publication by Associate Editor Y. Sun and Editor B. J. Nelson upon evaluation of the reviewers' comments. This work was supported in part by the Center for Automation Technologies and Systems under a Block Grant from the New York State Foundation for Science, Technology, and Innovation; in part by the Engineering Laboratory of the National Institute of Standards and Technology; and in part by the National Science Foundation Smart Lighting Engineering Research Center under Grant EEC-0812056.

J. D. Wason and J. T. Wen are with Rensselaer Polytechnic Institute, Troy, NY 12180 USA (e-mail: wasonj@rpi.edu; wenj@rpi.edu).

J. J. Gorman and N. G. Dagalakis are with the National Institute of Standards and Technology, Gaithersburg, MD 20899-8230 USA (e-mail: gorman@nist.gov; nicholas.dagalakis@nist.gov).

Color versions of one or more of the figures in this paper are available online at http://ieeexplore.ieee.org.

Digital Object Identifier 10.1109/TRO.2012.2200991

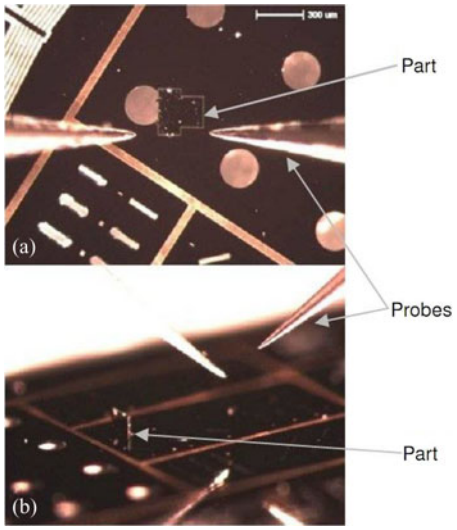

Fig. 1. Medium micropart (a) before (top view) (b) and after insertion (front view).

is intended to be a building block leading toward assembling complex spatial structures involving multiple parts. The experimental results demonstrate the stability of the primitive motions required to accomplish complex assembly tasks with the aid of vision feedback using multiple cameras.

There are microassembly techniques that do not use microgrippers, such as acoustic levitation [24], ultrasound ultrasonic vibration combined with electrostatic actuation [25], chopstick-like microhands [26], tweezers [27], [28] pushing-based planar manipulator with flat surfaces [29]–[32], and probe/finger-based manipulators [33]–[36]. Our approach is in the same spirit as the probe/finger-based method (particularly [34]), but our autonomous spatial manipulation (part flipping and insertion) capability using multiple-camera vision feedback represents an important advance toward automated assembly of complex micromechanisms.

II. Overall Approach

This paper focuses on a key task in the assembly of a spatial microstructure [37]: manipulation of a part with length scales of less than 1 mm. The manipulation is part of a more general single-part assembly procedure which is now discussed. We decompose the task into six task primitives: 1) system calibration, 2) part centering, 3) part grasping, 4) part rotation, 5) part insertion, and 6) part release. The current system uses a combination of preplanned sequences and closed-loop part manipulation to accomplish the manipulation. The plans are created manually based on experiments completed via teleoperation, and consist of either straight-line or simple geometrical motions. The vision feedback and part manipulation are used to correct for uncertainty that is inherent on this scale.

System Calibration

Since multiple cameras and probes are used for feedback, several calibration processes are required for the parameters in the system. They include intrinsic parameters of each camera (e.g., focal length), extrinsic parameters of the cameras (position and orientation relative to some reference frame), kinematics of the die stage, and kinematics of the probe stages. A reference grid pattern of straight gold lines are deposited on the die. The slope and intersections of the lines are used as features for camera and die-stage calibration. Probes are modeled as perfect cones. The straight line edges and the tip of the cone are used as features to estimate the pose of the probe relative to the cameras. All calibrations are performed at several fixed camera zoom levels and vision operations occur at these specific zoom levels.

Part Centering

The parts used in this research are part of a 25-μm silicon-on-insulator layer on the wafer. They are fabricated using the deep reactive ion etching process. The top layer is etched through to form parts. Then, the hydrofluoric acid (HF) wet etch process undercuts the oxide layer and releases the parts. Each part is attached to the wafer through small support tethers. The operator frees the part by breaking the tethers and places it in an open area on the die. The automated process starts by first using the overhead camera at a lower zoom (for a larger field of view) to locate the part. The die stage is then moved to position the part in the center of the camera view and aligned with the camera coordinate. The alignment process is performed at higher zoom to ensure the required higher accuracy for grasping (within 0.1° and 10 μm).

Part Grasping

The key step of this research is to coordinate the two probes to grasp and pick up the part. The top camera provides the xy position feedback and front camera provides the z position feedback of the probes relative to the part. Part grasping is formed by pressing the part from opposing sides on parallel edges. The contact force is measured based on the bending of the probe and is used to guide the probe motion. The goal is to develop the grasping strategy to securely grasp and lift the part while allowing part rotation (about the line between the probe contacts) to the vertical orientation.

Part Rotation

The rotation of the part into the vertical orientation is accomplished by pressing the part against a stationary probe to cause a rotation about the line between the probe contacts. With the contact with the stationary probe, the part orientation is fully defined (a three-point grasp). The stationary probe is mounted on a linear stage to allow it to be moved in and out of the workspace as needed. The force control set point needs to be chosen to allow a firm grasp during manipulation yet admit relative rotation along the line between the contacts. Since the probe locations are known, a planned trajectory sequence is used to perform the rotation without the vision feedback. The part is rotated slightly past the vertical so that it is more easily detected with the

overhead camera. The orientation is corrected to vertical during the final insertion.

Insert Part

After the part has been rotated, the top camera at a high zoom level is used to provide vision feedback to the probes to position the part above the slot, with the bottom edge of the part aligned with the slot. The part is then lowered into the slot using a preplanned motion sequence.

Part Release

The part is released by rapidly pulling the probes away from the part in opposite directions. Since the part is constrained by the slot, the probe motion breaks the adhesion force at the contact. Therefore, there is no need for the snap fasteners used in other methods for part release.

III. Compliant Grasp With Two Probes

Grasping, manipulating, and rotating the part with two probes is the most challenging part of the assembly process. It is similar to the manipulation of a light fragile part using two fingers. The fingers need to be coordinated to impart a squeeze hard enough to avoid dropping the part, but not too hard as to buckle the part causing it to break or lose the grasp resulting in the part being ejected from the workspace. The magnitude of squeeze force also needs to be carefully regulated to maintain a firm grip of the part when moving it around but still gentle enough to allow the part to rotate when it is pressed against the stationary probe. In contrast with macroscale robots, the light weight of the part and relatively slow motion only requires the consideration of kinematics. In this section, we will present the motion and force control of a microscale (less than 1 mm) part using two probes and the robustness of the scheme in the presence of misalignment. The force sensing required in the squeeze force control will be estimated using vision-based measurement of the bending of the probes.

A. Kinematics-Based Motion and Force Control

Consider two probes contacting a part, as shown in Fig. 2. Let C be an Euclidean frame fixed with respect to the part. In this paper, we only use the Cartesian motion of the probes, and the contacts are modeled as point contacts with friction. Following the convention in [38], the differential kinematics are then given by

$$AV_c = Ju + Hw \tag{1}$$

where

$$A := \begin{bmatrix} A_L \\ A_R \end{bmatrix}, \quad J := \begin{bmatrix} J_L & 0 \\ 0 & J_R \end{bmatrix}, \quad H = \begin{bmatrix} H_L & 0 \\ 0 & H_R \end{bmatrix}$$

$$V_c := \begin{bmatrix} \omega_c \\ v_c \end{bmatrix}, \quad u = \begin{bmatrix} u_L \\ u_R \end{bmatrix}, \quad w = \begin{bmatrix} w_L \\ w_R \end{bmatrix}$$

(ω_c, v_c) is the spatial velocity of C, (u_L, u_R) are the commanded Cartesian velocity of the probes, (w_L, w_R) are the relative rotations between the probes and the part, and

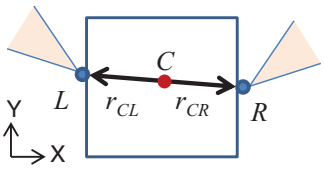

Fig. 2. Kinematics of two probes interacting with a part.

$$A_L = \begin{bmatrix} I_{3\times3} & 0_{3\times3} \\ -r_{CL}\times & I_{3\times3} \end{bmatrix}, \quad A_R = \begin{bmatrix} I_{3\times3} & 0_{3\times3} \\ -r_{CR}\times & I_{3\times3} \end{bmatrix} \tag{2}$$

$$J_L = J_R = \begin{bmatrix} 0_{3\times3} \\ I_{3\times3} \end{bmatrix}, \quad H_L = H_R = \begin{bmatrix} I_{3\times3} \\ 0_{3\times3} \end{bmatrix}. \tag{3}$$

Note that A is of full column rank; therefore, its left-inverse and annihilator may be written as

$$A^\dagger = \frac{1}{2}\begin{bmatrix} A_L^{-1} & A_R^{-1} \end{bmatrix}, \quad \widetilde{A} = \begin{bmatrix} A_L^{-1} & -A_R^{-1} \end{bmatrix}. \tag{4}$$

To obtain the constraint equation of the closed kinematic chain, we apply $\widetilde{A}$ to both sides of (1):

$$\widetilde{A}Ju + \widetilde{A}Hw = 0. \tag{5}$$

The orientation portion of (5) does not involve u and implies

$$w_L = w_R. \tag{6}$$

The translational portion of (5) is

$$\begin{aligned} &u_L - u_R + r_{CL} \times w_L - r_{CR} \times w_R \\ &\quad = u_L - u_R + (r_{CL} - r_{CR}) \times w_L = 0. \end{aligned} \tag{7}$$

Parameterize w_L (and w_R) as

$$w_L = w_R = \begin{bmatrix} e_{LR} & e_{LR_1}^\perp & e_{LR_2}^\perp \end{bmatrix} \begin{bmatrix} w_1 \\ w_2 \\ w_3 \end{bmatrix} \tag{8}$$

where e_{LR} is the unit vector pointing from contact R to contact L, $e_{LR_1}^\perp$ is any unit vector perpendicular to e_{LR} (chosen to be on the plane of the part), and $e_{LR_2}^\perp := e_{LR} \times e_{LR_1}^\perp$. Substituting into (7), we get

$$u_L - u_R = \ell \begin{bmatrix} 0 & e_{LR_2}^\perp & -e_{LR_1}^\perp \end{bmatrix} \begin{bmatrix} w_1 \\ w_2 \\ w_3 \end{bmatrix} \tag{9}$$

where ℓ is the length of the line segment from L to R. We can now solve for w_2 and w_3:

$$\begin{bmatrix} w_2 \\ w_3 \end{bmatrix} = \begin{bmatrix} (e_{LR_2}^\perp)^T \\ -(e_{LR_1}^\perp)^T \end{bmatrix} \frac{u_L - u_R}{\ell}. \tag{10}$$

The variable w_1 is arbitrary, corresponding to the null space motion of $\widetilde{A}H$ (rotation about the line between the contacts). This DOF allows the rotation of the part by pressing the part with the stationary probe [39].

For the part motion, multiply both sides of (1) by $A^\dagger$ to get

$$V_C = A^\dagger J u + A^\dagger H w. \tag{11}$$

The rotational portion only depends on w. Using the solution from the constraint equation, we have

$$\omega_c = \frac{1}{2}(w_L + w_R). \tag{12}$$

Representing ω_c as

$$\omega_c = \begin{bmatrix} e_{LR} & e^\perp_{LR_1} & e^\perp_{LR_2} \end{bmatrix} \begin{bmatrix} \omega_{c_1} \\ \omega_{c_2} \\ \omega_{c_3} \end{bmatrix}$$

we have

$$\omega_{c1} = w_1 \tag{13}$$

$$\begin{bmatrix} \omega_{c2} \\ \omega_{c_3} \end{bmatrix} = \begin{bmatrix} (e^\perp_{LR_2})^T \\ -(e^\perp_{LR_1})^T \end{bmatrix} \frac{u_L - u_R}{\ell} \tag{14}$$

where w_1 corresponds to the rotation about the line between the contacts. The translational portion is given by

$$v_c = \frac{1}{2}(u_L + u_R) + (r_{CL} + r_{CR}) \times \omega_c. \tag{15}$$

If we choose C to be the midpoint on the line between the contacts, then $r_{CL} = -r_{CR}$ is along e_{LR} and, as expected, w_1 will have no effect on v_C. Putting both angular and linear velocities together (except for ω_{c1} which is not controlled by the probe motion directly), we have (with C chosen along e_{LR})

$$\begin{bmatrix} \omega_{c2} \\ \omega_{c3} \\ v_c \end{bmatrix} = \underbrace{\begin{bmatrix} (e^\perp_{LR_2})^T & -(e^\perp_{LR_2})^T \\ -(e^\perp_{LR_1})^T & (e^\perp_{LR_1})^T \\ \frac{1}{2} I_{3\times 3} & \frac{1}{2} I_{3\times 3} \end{bmatrix}}_{J_T} \begin{bmatrix} u_L \\ u_R \end{bmatrix}. \tag{16}$$

The Jacobian matrix J_T is a 5×6 full column rank matrix. Proportional feedback may be used to control the corresponding orientation and position:

$$\begin{bmatrix} u_L \\ u_R \end{bmatrix} = -J_T^\dagger K_m \begin{bmatrix} \phi - \phi_{\text{des}} \\ x_c - x_{c_{\text{des}}} \end{bmatrix} \tag{17}$$

where $(x_c, x_{c_{\text{des}}})$ are the measured and desired positions of C, and $(\phi, \phi_{\text{des}})$ are the measured and desired angles corresponding to $(\omega_{c2}, \omega_{c3})$, respectively.

For the squeeze force, first recognize that the contact spatial force (torque and force), i.e., $F = \begin{bmatrix} F_L^T & F_R^T \end{bmatrix}^T$, is complementary to the contact motion, i.e.,

$$H_L F_L = H_R F_R = 0 \tag{18}$$

or the contact spatial forces only consist of forces

$$F_L = \widetilde{H}_L^T \eta_L, \quad F_R = \widetilde{H}_R^T \eta_R \tag{19}$$

where $\widetilde{H}_{L/R}$ is the annihilator of $H_{L/R}$:

$$\widetilde{H}_L = \widetilde{H}_R = \begin{bmatrix} 0_{3\times 3} & I_{3\times 3} \end{bmatrix} \tag{20}$$

and η_L and η_R are the contact forces. The forces propagate to C to cause part motion (translation only)

$$F_C = A^T F = A^T \widetilde{H}^T \underbrace{\begin{bmatrix} \eta_L \\ \eta_R \end{bmatrix}}_{\eta}$$

$$= \begin{bmatrix} r_{CL}\times & r_{CR}\times \\ I_{3\times 3} & I_{3\times 3} \end{bmatrix} \begin{bmatrix} \eta_L \\ \eta_R \end{bmatrix}. \tag{21}$$

The component of the contact force η that does not cause motion (i.e., in the null space of $A^T \widetilde{H}^T$) imparts a "squeeze" to the part

$$\mathcal{N}(A^T \widetilde{H}^T) = \gamma \begin{bmatrix} e_{LR} \\ -e_{LR} \end{bmatrix}. \tag{22}$$

A common and effective force control strategy is integral force feedback (see, e.g., [40]), where the applied squeeze force control (the control that does not cause motion) is a negative feedback of the measured squeeze force error. Assuming linear compliance of the part, the integral force control (note that the input is the commanded velocity) becomes

$$u_L = -u_R = -k_f (f_s - f_{s_{\text{des}}}) e_{LR} \tag{23}$$

where f_s is the scalar component of the squeeze force η, and $f_{s_{\text{des}}}$ is the desired squeeze force level.

Combining the motion and force controllers [see (17) and (23)] together, we obtain the controller for the probe velocity that we use for grasping, manipulation, and rotation of the part:

$$\begin{bmatrix} u_L \\ u_R \end{bmatrix} = -J_T^\dagger K_m \begin{bmatrix} \phi - \phi_{\text{des}} \\ x_c - x_{c_{\text{des}}} \end{bmatrix} - k_f \begin{bmatrix} -(f_s - f_{s_{\text{des}}}) e_{LR} \\ (f_s - f_{s_{\text{des}}}) e_{LR} \end{bmatrix}. \tag{24}$$

The xy components of the measured part position x_c are obtained from the top camera image. The z component of x_c is obtained from the side camera. The unit vector between the contacts, i.e., e_{LR}, is obtained based on the probe tip positions. The desired part orientation and position $(\phi_{\text{des}}, x_{c_{\text{des}}})$ is specified by the planner for each task primitive. The squeeze force f_s is estimated based on probe deformation obtained from vision, as presented in Section III-C.

B. Two-Probe Grasp With Third Probe for Out-of-Plane Rotation

The Jacobian derived for the two-probe grasp is rank-deficient in that it is only a 5×6 matrix. This result means that while there are six actuated inputs, only five of the spatial velocities can be directly affected by the two-probe grasp. The solution to this problem is to use a third probe that is pressed against the surface of the part at some distance normal to the vector e_{LR}. This probe is assumed to be fixed in space. Define the vector r_{C3} as the vector from point C to the contact point of the third probe. From the expressions derived earlier, we can write the velocity of the contact point of the third probe on the part as

$$V_3 = V_c + w_c \times r_{C3} = 0. \tag{25}$$

Substitute (10) into (25), and rewrite (25) and (15) to separate out u_L and u_R:

$$u_L + u_R = 2r_{C3} \times w_c \tag{26}$$

$$u_L - u_R = \ell \begin{bmatrix} e_{LR_2}^{\perp} & -e_{LR_1}^{\perp} \end{bmatrix} \begin{bmatrix} \omega_{c_2} \\ \omega_{c_3} \end{bmatrix}. \tag{27}$$

By subtracting or adding (26) and (27) from each other, two independent expressions for u_R and u_L are obtained. These equations define the relationship between the input of the two controlled grasp probes and the third probe fixture

$$u_L = r_{C3} \times w_c + \frac{1}{2}\ell \begin{bmatrix} e_{LR_2}^{\perp} & -e_{LR_1}^{\perp} \end{bmatrix} \begin{bmatrix} \omega_{c_2} \\ \omega_{c_3} \end{bmatrix} \tag{28}$$

$$u_R = r_{C3} \times w_c - \frac{1}{2}\ell \begin{bmatrix} e_{LR_2}^{\perp} & -e_{LR_1}^{\perp} \end{bmatrix} \begin{bmatrix} \omega_{c_2} \\ \omega_{c_3} \end{bmatrix}. \tag{29}$$

This can be written in matrix form to develop a Jacobian for this condition. The velocity of the part in this configuration can be obtained from (25) as

$$C_1 = \begin{bmatrix} e_{LR} & e_{LR_2}^{\perp} & e_{LR_1}^{\perp} \end{bmatrix} \tag{30}$$

$$C_2 = \frac{1}{2}\begin{bmatrix} 0_{3x1} & e_{LR_2}^{\perp} & -e_{LR_1}^{\perp} \end{bmatrix} \tag{31}$$

$$\begin{bmatrix} \omega_{c_1} \\ \omega_{c_2} \\ \omega_{c_3} \end{bmatrix} = \underbrace{\begin{bmatrix} r_{C3}^{\times} C_1 + \ell C_2 \\ r_{C3}^{\times} C_1 - \ell C_2 \end{bmatrix}^{-1}}_{J_{T_3}} \begin{bmatrix} u_L \\ u_R \end{bmatrix}. \tag{32}$$

The prismatic velocity portion of the Jacobian with third probe contact is dependent on ω_c. When in contact with the third probe only, the orientation can be controlled.

C. Vision-Based Contact Force Estimation

Tungsten probes are used to grasp and manipulate the microparts being assembled. Tungsten probes are tough, cheap, and have a high Young's modulus. The geometry of the probe is shown in Fig. 3. The cross section of the probe is circular. The probe is long compared with its cross section dimension; we can, therefore, model it as an Euler–Bernoulli beam [41]. In a static equilibrium, the probe deflection is given by

$$\frac{d^2}{dx^2} EI(x) w''(x) = 0, \quad 0 \le x \le \ell_0 \tag{33}$$

where w is the bending deflection displacement of the probe at location x, E is Young's modulus of Tungsten, $I(x)$ is the area moment of inertia, and ℓ_0 is the length of the probe. The boundary conditions, i.e., fixed at $x = \ell_0$, a transverse force F applied to the probe tip, and zero moment at the probe tip $x = 0$, are given as follows:

$$w(\ell_0) = w'(\ell_0) = 0, \quad w''(0) = 0, \quad \frac{dEIw''}{dx}(0) = F \tag{34}$$

where F is the transverse force applied to the probe tip.

We are interested in determining the force exerted onto the probe by measuring its tip deflection $w(0)$ using vision. By solving (33) and applying the boundary condition [41], the tip deflection is related to the applied force by

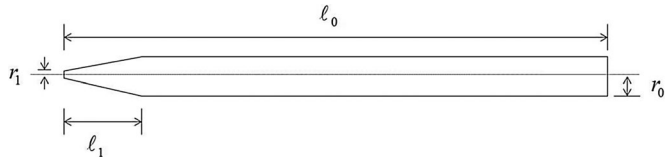

Fig. 3. Diagram of probe shape and applied bending force.

$$w(0) = \underbrace{\left(\frac{1}{E} \int_0^{\ell_0} \int_{\ell}^{\ell_0} \frac{s}{I(s)}\, ds\, d\ell \right)}_{K_b} F. \tag{35}$$

This relationship holds true for the probe bending in the transverse (y and z) directions under the small strains encountered during micrograsping.

The cameras are used to measure the probe tip bending vector δ_b in the probe transverse direction. From the bending stiffness, K_b from (35), the bending force may be estimated as

$$F_b = K_b \delta_b. \tag{36}$$

To find the squeeze force, we solve the force balance at the contact, including the axial force on the probe. Since the probe is a thin rod with high axial stiffness, we shall assume the probe is infinitely rigid in the axial direction for the small forces encountered during micrograsping

$$F_b + f_a x_{\text{probe}} + f_s e_{LR} = 0 \tag{37}$$

where f_a is a scalar force value along the axial direction of the probe x_{probe}. We used finite-element models to calculate the stiffness of the various parts manipulated by the workstation probes. It turns out that the lowest stiffness of the microparts is approximately 1000 times greater than the stiffness of the manipulation probes; therefore, we expect no significant deformation of the microparts during manipulation. Since F_b and x_{probe} are orthogonal, we may solve for the squeeze force as

$$f_s = -\frac{\|F_b\|^2}{F_b^T e_{LR}}. \tag{38}$$

When the top camera is used, only the planar projection of δ_b is measured, i.e.,

$$\delta_b = \delta_{b_{xy}} + \delta_{b_z} z_o \tag{39}$$

where $\delta_{b_{xy}} = (I - z_o^T z_o)\delta_b$ is the measured planar projection of δ_b, and δ_{b_z} is an additional unknown of δ_b in the world z-direction, z_o. The force balance equation then becomes

$$K_b \delta_{b_{xy}} + K_b \delta_{b_z} z_o + f_a x_{\text{probe}} + f_s e_{LR} = 0 \tag{40}$$

and may be used to solve for (δ_{b_z}, f_a, f_s), provided $(K_b z_o, x_{\text{probe}}, e_{LR})$ are independent.

The configuration with the probes in direct opposing directions (i.e., e_{LR} and x_{probe} are collinear) should be avoided as f_s cannot be uniquely determined. This configuration is also undesirable as it does not utilize the compliance of the probe in the bending direction—the high stiffness in the axial direction

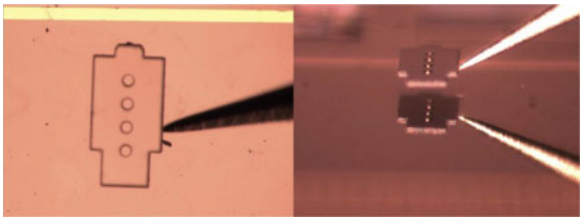

Fig. 4. Part supported by a single probe.

makes the grasp much less robust, where small misalignment would cause failure of the grasp.

For our experiment, we have used commercially available tungsten probes. Each probe has a circular cross section with shaft diameter $r_0 = 0.255$ mm and tip radius $r_1 = 10$ μm. The length of the tip portion of the probe is $\ell_1 = 2.8$ mm, tapering linearly from r_0 to r_1. After clamping, the length of the probe is $\ell_0 = 25.4$ mm. The radius of the probe may be written as

$$r(x) = \begin{cases} r_1 + \dfrac{r_0 - r_1}{\ell_1} x, & 0 \le x \le \ell_1 \\ r_0, & \ell_1 < x \le \ell_0. \end{cases} \tag{41}$$

The area moment of inertia for a circular rod is

$$I(x) = \frac{1}{4}\pi r(x)^4.$$

Young's modulus of Tungsten is $E = 400$ GPa. The bending stiffness is calculated to be $K_b = 217.6$ N/m and the axial stiffness to be $K_a = 848\,000$ N/m.

D. Contact Adhesion

At the microscale, a set of adhesion effects become significant compared with friction (when sliding on a surface), gravity, and inertia that dominate the macroscale. Fig. 4 shows that the adhesion is in fact strong enough for the part to stick to the probe. This force consists of primarily three sources: van der Waals, capillary attraction, and electrostatic. Because the parts and probes are conductive, we assume that the electrostatic force is negligible.

The van der Waals attraction is composed of two separate forces: the attraction caused by the electrostatics in sphere-plate contact and the additional adhesion caused by the elastic and plastic flattening of the probe tip when it is pressed against the part by an external force [42]. This occurs when the probes press the part in a grasp.

We model the extra surface contact area between the probes and part as the spherical tungsten tip flattened while in contact with a planar silicon body [43]. The radius of the contact Hertzian ball is given by

$$a = \left(\frac{3Ft_1}{t_2}\right)^{\frac{1}{3}}, \quad t_1 = \frac{1-\nu_1^2}{E_1} + \frac{1-\nu_2^2}{E_2}, \; t_2 = \frac{8}{d_1} \tag{42}$$

where E is Young's modulus, ν is the Poisson ratio, with subscript 1 for the probe and 2 for the part, d_1 is the diameter of the tungsten spherical tip, and F is the applied normal force. The maximum pressure between the part and probe is given by

$$P_{\max} = \frac{3F}{2\pi a^2}. \tag{43}$$

Based on the vision-based force measurement described before, the normal force between the probe and part in a secure grasp is typically around 5 mN. Using properties of tungsten and silicon, $E_1 = 400$ GPa, $E_2 = 100$ GPa $\nu_1 = 0.22$, $\nu_2 = 0.28$, $d_1 = 20$ μm, and $F = 5$ mN, the Hertzian contact model predicts a relatively large contact area $a = 757$ nm and a very high maximum pressure $P_{\max} = 4.16$ GPa, which is well above the yield stress of tungsten, i.e., 1.51 Gpa. This indicates that the elastic and plastic flattening of the probe tip is reasonable. Other models commonly used for contact areas are for relative low contact pressure. Here, the high contact pressure shows that Hertzian contact is a good approximation.

The van der Waals force can be calculated using the contact radius from the Hertzian contact equations [42]. The force due to the initial sphere-plate contact is given by

$$F_{vdw} = \frac{hr}{8\pi z^2} \tag{44}$$

where $h = 7$ eV is the van der Waals constant, $z = 0.4$ nm is the van der Waals distance for silicon, and $r = 10$ μm is the tip radius. This results in $F_{vdw} = 2.8$ μN. When the flat contact has been formed from the external grasp pressure, the additional force is calculated as

$$F_{vdw,def} = \frac{ha^2}{8\pi z^3} \tag{45}$$

where a is the radius of the contact sphere from (42). With the 5-mN normal force at the contact, this works out to be 400 μN. The high level of extra adhesion requires large probe deformation, which needs to be generated with sufficiently high applied pressure. This means that simply contacting the part with a light touch will not create a strong adhesion force. Force must first be applied at a relatively high level to form an enlarged contact area in order to create stiction.

Capillary attraction also provides adhesion between the part and probe. In a normal humid environment, there is a thin layer of water that causes capillary attraction on most surfaces. The capillary force between a probe and part can be estimated as [44]

$$F_{\text{cap}} \approx 4\pi r \sigma_s \tag{46}$$

where $r = 10$ μm is the probe radius, and $\sigma_s = 0.073$ N/m is the surface tension of water, resulting in the estimated capillary force $F_{\text{cap}} = 9.17$ μN.

While we have presented an estimation of contact adhesion forces, in general, these forces are treated as disturbances rather than an important physical effect during manipulation. Part release is complicated by the contact adhesion; however, with high probe acceleration, it is possible to break the adhesion and release the part.

IV. Vision Sensing

The microassembly process that is described in Section II uses vision feedback to locate the probes, die, and parts, as well as to position and move them to desired locations. Joint position feedback alone is not sufficient to achieve the required accuracy. The vision feedback system is based on two high-resolution

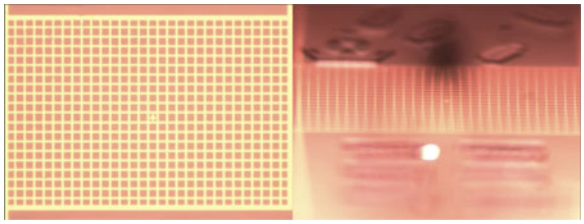

Fig. 5. Camera calibration pattern from top (left) and front views (right).

cameras. These cameras are both Basler A631F[1] cameras, with actuated zoom lenses providing between 2× to 4× zoom. The Basler A631F Firewire camera has a maximum resolution of 1392 × 1040 pixels, with a large 1/2-in progressive scan charge-coupled device (CCD) sensor. When combined with the actuated zoom lenses, this provides a working resolution of between 3 and 1.5 μm per pixel depending on the zoom level. The lenses have been augmented with stepper motors to provide automated zoom capabilities. One camera is configured as an overhead camera, while another camera provides a front view approximately 20° off horizontal. The two cameras are calibrated with respect to each other by using a reference grid designed into the die. This configuration is similar to other microassembly work cells [22], [45].

The first step in system operation is camera calibration. The intrinsic camera parameters are predetermined; therefore, we only calculate the extrinsic position and orientation of the cameras at startup. Fig. 5 shows the reference grid used for calibration in the top and front views. The top camera is assumed to be telecentric and perfectly aligned to the die plane. Over the height of 500 μm for the system workspace, this is valid to within approximately 2 μm. The front camera is calibrated using a standard pinhole camera model [46]. The focal length is predetermined and is long enough that the front camera is also effectively telecentric. From the image, it is clear that approximately six horizontal grid lines are in focus in the front-view camera. This corresponds to an area approximately 500 μm × 500 μm × 2000 μm of 3-D calibrated workspace, as shown in Fig. 6.

The use of vision feedback instead of other sensing modalities used in past work has many advantages. Vision systems are robust in that they are not easily damaged, in contrast with, e.g., force sensors. Vision does not come in contact and, hence, does not interfere with workpieces. Vision sensing provides a complete view of the workspace from which information on the state of the system may be extracted. The cameras in use on the system are low cost but provide micrometer-level resolution. Finally, vision information is sensitive to instantaneous position—there is no motion-induced hysteresis (memory of past motion), such as in force sensors.

The different features in the workspace require different lighting conditions in order to be extracted by computer-vision

[1]Certain commercial products and processes are identified in this paper to foster understanding. Such identification does not imply recommendation or endorsement by the National Institute of Standards and Technology, nor does it imply that the products and processes identified are necessarily the best available for the purpose.

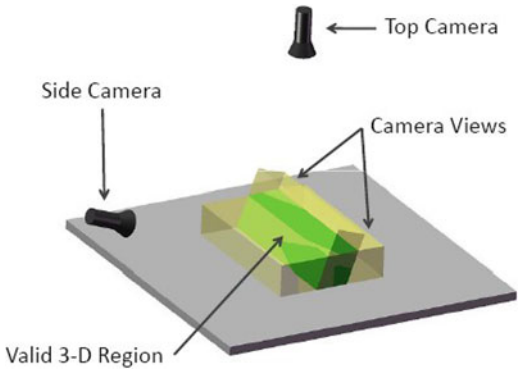

Fig. 6. Calibrated microscope envelope showing individual camera workspaces and combined camera workspace.

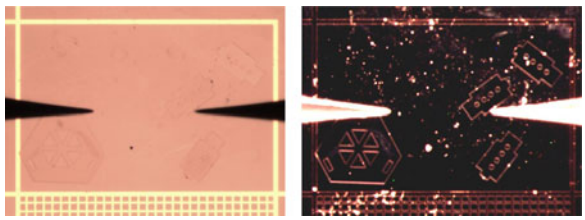

Fig. 7. Parts, probe, and die illuminated with coaxial (left) and ring (front) light sources.

algorithms. The overhead microscope is equipped with a coaxial illuminator and a ring light. The coaxial illuminator is used to detect the gold reference marks on the die, the probes, and the slots for insertion. Due to the parts being made out of the same material as the die, they are not directly visible with this illumination. The ring light illumination highlights the edge of the parts and is used for part detection. Fig. 7 shows the same view with the two different illumination sources. The front camera is equipped with a separate ring light.

A key step in vision-based sensing is the extraction of features of interest from the acquired image. However, small dust particles tend to collect on the surface, erroneously triggering standard feature detectors. Therefore, we employ a template matching scheme using direct template-image convolution [47]. Templates are generated from knowledge of the shape of the item being tracked and then rotated and convolved with the images to determine the best match.

The template matching method used in the microassembly system to locate parts is facilitated by the use of a ring light illumination, which causes edges to "glow." There are areas on the die that are much brighter in the image than the feature of interest. To enhance noise immunity, we choose the Laplacian-of-Gaussian [46] approach for line detection. The intensity of the edges is inherently Gaussian. A template is, therefore, generated by extruding a 2-D Gaussian-like function along each line. To enhance contrast, we use a "Mexican hat" profile instead of the Gaussian.

The highlighted edges formed by the ring light illumination are used to detect the part and probes in various elements. Fig. 8 shows a surface representation of the part template intensity map used to locate the part. This template is rotated and convolved

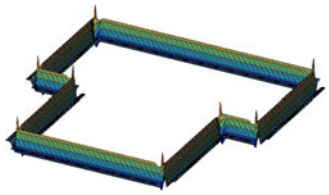

Fig. 8. Part detection template.

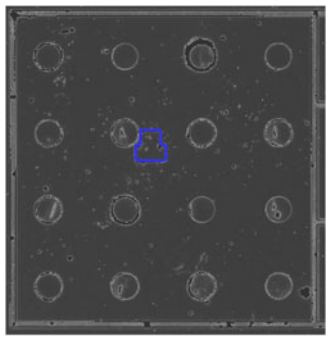

Fig. 9. Part search at low zoom.

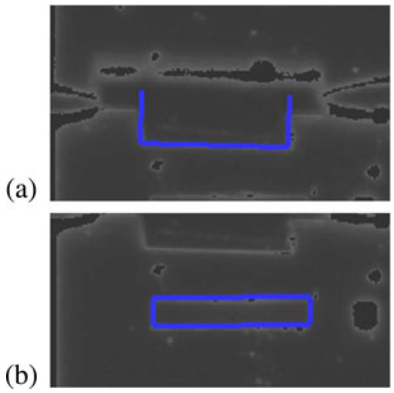

Fig. 10. (a) Part and (b) slot detection at high zoom for insertion.

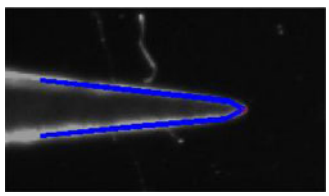

Fig. 11. Probe template.

to find the best matching orientation and position. Fig. 9 shows the results of a search with an image of the workspace and blue lines representing the located part. Fig. 10 shows images of the bottom of the part and the insertion slot and their corresponding matched templates. Fig. 11 shows the probe template matched with an image of the probe.

The front camera is used to measure the height of the probes and part in the workspace. Due to the inherent error in the calibration, it is difficult to achieve the accuracy of a few micrometers in height required to grasp the 25-μm edge of the part when the part is lying flat on the surface. Instead, we exploit the fact that the polished silicon surface is nearly a perfect mirror, providing a detailed reflection. The separation between the probe and its reflection is used to precisely determine its height. Fig. 12 shows the reflection of the probes with the front camera in high zoom.

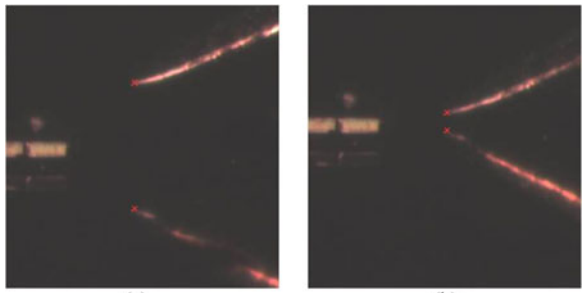

Fig. 12. Probes and its reflection [in (a)] are used to lower the probe to the correct height for part grasping [in (b)].

Vision processing is a computationally expensive operation using the methods necessary to detect the parts and probes. The camera takes approximately 200 ms for image acquisition. For the results reported in this paper, the image is transmitted to a quad-core Intel central processing unit with 12 Gb of random access memory using Gigabit Ethernet. The processing of each frame takes 3–4 s depending on the number of pattern matching required. We have recently upgraded to a new 512-core graphics processing unit (GPU)-based image-processing system. The computation time is dramatically reduced to less than 50 ms, making the image acquisition now the bottleneck. The GPU implements the "Mexican hat" template generation, fast Fourier transform, and least-squares image matching using NVidia CUDA and OpenCV software.

V. Experimental Demonstration of Insertion Process

A. Overview of Microassembly Testbed

The microassembly system used in this research is a combination of hardware and software configured for telerobotic, operator-assisted, and fully automated assembly tasks. Several different components have been integrated to produce an effective system. Fig. 13 shows the closeup view of the microassembly testbed. The major components of the system are as follows.

1) The tungsten probes (GGB Industries ST-20-10) are mounted on two 3-DOF Thorlabs NanoMax 600 positioners in an opposed configuration (1.2-μm step size, 2.4-μm repeatability).
2) A 3-DOF die stage (x-y-θ) consisting of a Newport CR4524 X-Y stages with EncoderDriver DC motor actuators and an OWIS Qmbh B-0308143X rotational stage with stepper motor (2-μm linear accuracy, $<$1-mdeg rotation accuracy).
3) There are two 1.2-Megapixel C-mount microscope Firewire cameras with actuated zoom. These cameras are both Basler A631F cameras. The top camera has an actuated colluminated 16$\times$ precision zoom lens. The side camera uses an Edmund VZM450 zoom lens. The Basler

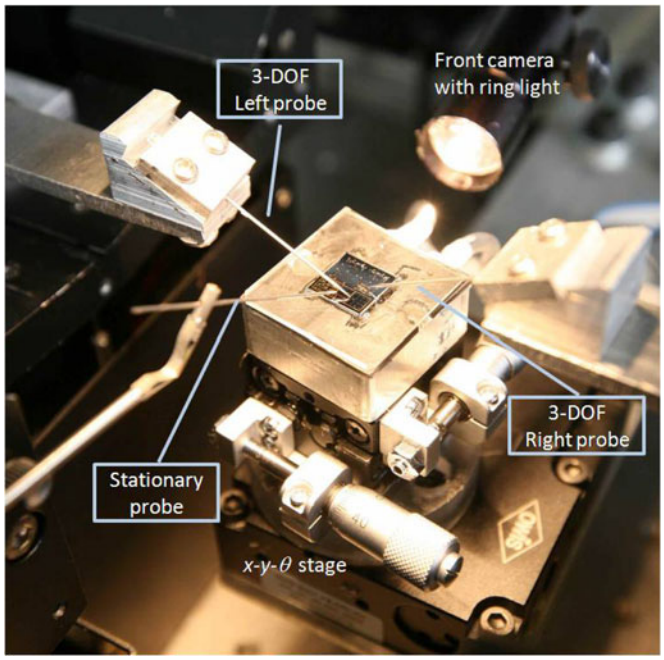

Fig. 13. Closeup view of the microassembly experimental testbed.

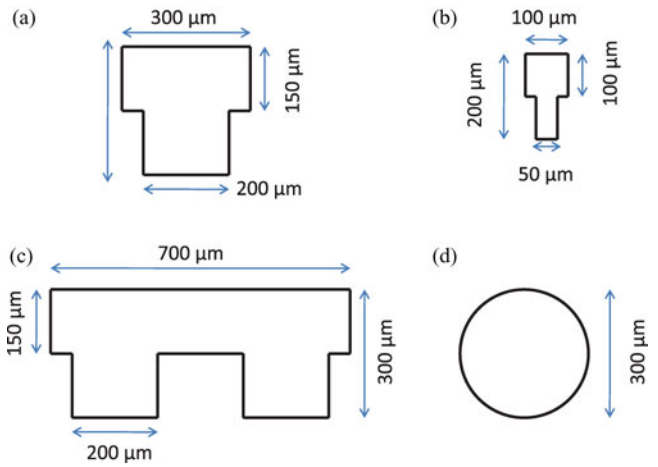

Fig. 14. Dimensions of different size parts used in experiments: (a) Medium. (b) Small. (c) Double-tab. (d) Ball lens.

A631F Firewire camera has a maximum resolution of 1392 × 1040 pixels, with a large 1/2-in progressive scan CCD array. When combined with the zoom lens, it provides a working resolution of between 3 and 1.5 µm depending on the zoom level limited by the digital camera. The lenses have been augmented with stepper motors to provide automated zoom capabilities. These lenses have a constant working distance over the entire zoom range. One camera is configured as an overhead camera, while another camera provides a side view approximately 20° off horizontal.

4) There are custom control electronics with software based on MATLAB, C#, C++, and CUDA.

The system is designed around two actuated probe manipulators operating over a silicon die containing the device being assembled. The two manipulators are sharp-tipped probes (20-µm diameter) that are designed to manipulate small silicon parts. The die itself is mounted on a 3-DOF (planar translation and rotation) stage mounted between the two-probe stages. The die stage allows the die to be moved into and out of the relatively limited work space of the probes—the range of motion in any direction is only approximately 4 mm. With the combination of the motion of the probes and the motion of the die, manipulation can take place at any location on the 10 mm × 10 mm die. The kinematic relationship between the various components in the system is determined through an automated vision-based calibration procedure [39].

B. Vision-Based Motion and Force Control

We first focus on stably grasping the part and moving it around. In the example experiment, we conduct two moves that requires coordinated motion and force control. The beginning of the experiment involves using the probes grasping the part, lifting it up by about 80 µm, and centering it (with the mid-point of the part at $x = y = 0$ and $\theta = 0$, the rotation angle about z). The first move involves moving the midpoint of the part to $x =$ 80 µm, $y = -80$ µm, and rotating the part by $\theta = 15°$. The second move involves moving the midpoint of the part back to $x = 0$ µm, $y = -0$ µm, and rotating the part to $\theta = 0°$. The relatively small motion ranges are chosen to ensure the part remains within the field of view of the top camera. Because the die stage is actuated, only small motion by the probes is necessary for the fine adjustment during insertion. Throughout the move, the force set point is 5 mN. This set point is chosen to maintain a robust grasp during motion. Parts of four different geometries are used, as shown in Fig. 14. The top camera images of the probes grasping these parts are shown in Fig. 15. The motion and force results for the example moves with the medium part are shown in Figs. 16 and 17. The results of other parts are similar and may be found in [48]. Currently, the operation is quasi-static; therefore, the completion time is horizontal "sample" axis that denotes the number of the move steps where the contact force is measured by vision at each step. The bottleneck is the vision processing which has recently been upgraded to a GPU-based system. The position converges to the specified set point in each motion segment. The force converges to the force set point in the first segment and maintains around the set point in the second segment. The force is estimated by measuring the deflection of the probe using the cameras. This procedure is noisy and only provides a coarse measurement; therefore, the estimated value shows some level of oscillation. However, the force measurement is sufficient for a stable grasp, as shown in the experiment. Due to the camera resolution and probe motion resolution limits, the final positioning accuracy is less than 5 µm for the prismatic directions and less than 0.1° for the part orientation. The sensing is limited by the digital pixel sampling of the camera and the vision template matching. The movements of the part are relatively small because in an actual manipulation system, large range of motion in the x and y plane is not required. This is because the substrate will translate and rotate under the workspace on the die stage. This means that what is required for part manipulation is small final positioning rather

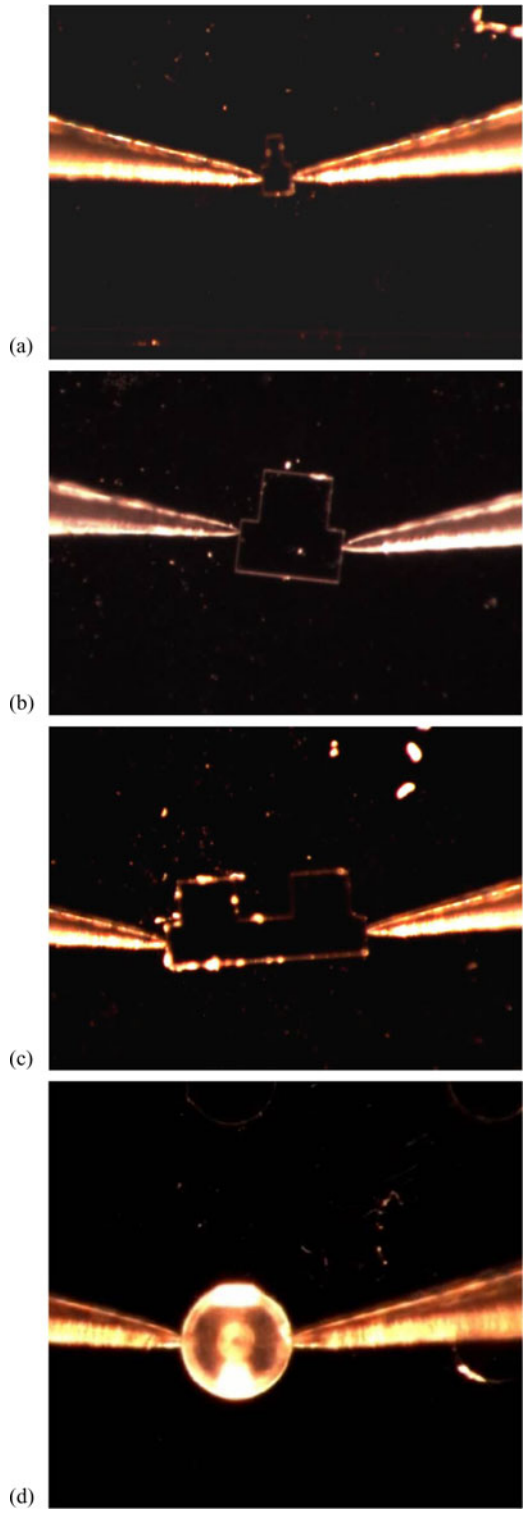

Fig. 15. Microscope captures of different parts in grasp. (a) Small. (b) Medium. (c) Double-tab. (d) Ball lens.

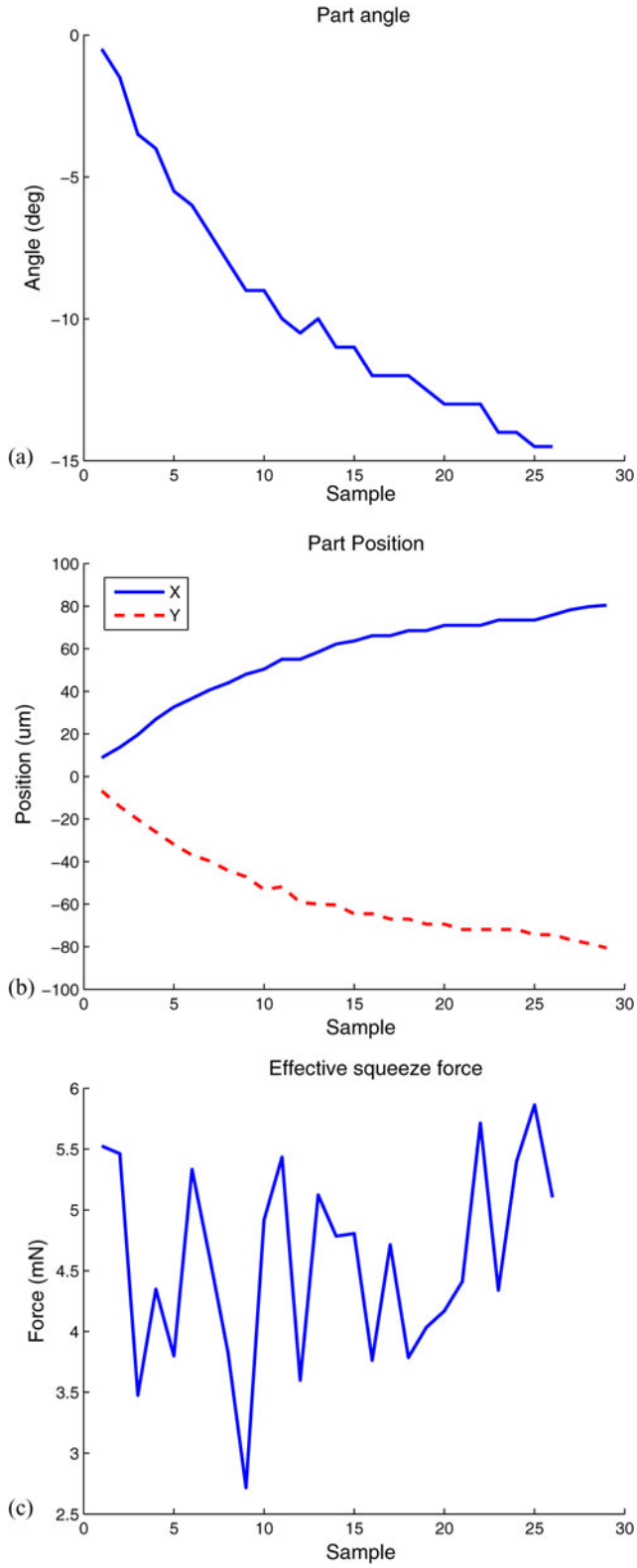

Fig. 16. Medium part first motion (a) angle (b) position (c) grip force versus sample.

than large motions. Fig. 18 shows repeated motions to demonstrate that a stable grasp is maintained after cycling through the same motion path.

We have manipulated parts as small as 200 μm × 100 μm up to approximately 1 mm × 1 mm. It is likely that smaller and larger parts can be manipulated. The main limitation for small parts is the ability of the camera to resolve the parts. The limitation for large parts is the size of the camera field of view, which needs to include both probe contacts.

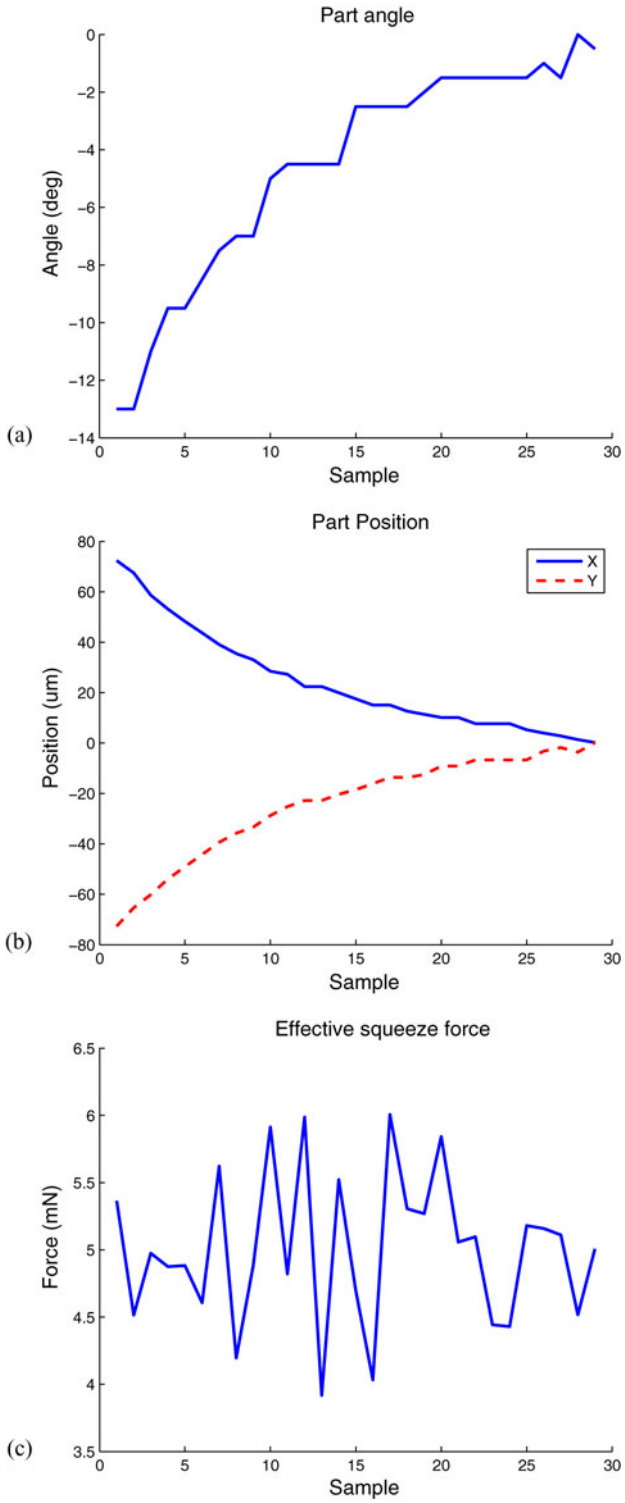

Fig. 17. Medium part second motion (a) angle (b) position (c) grip force versus sample.

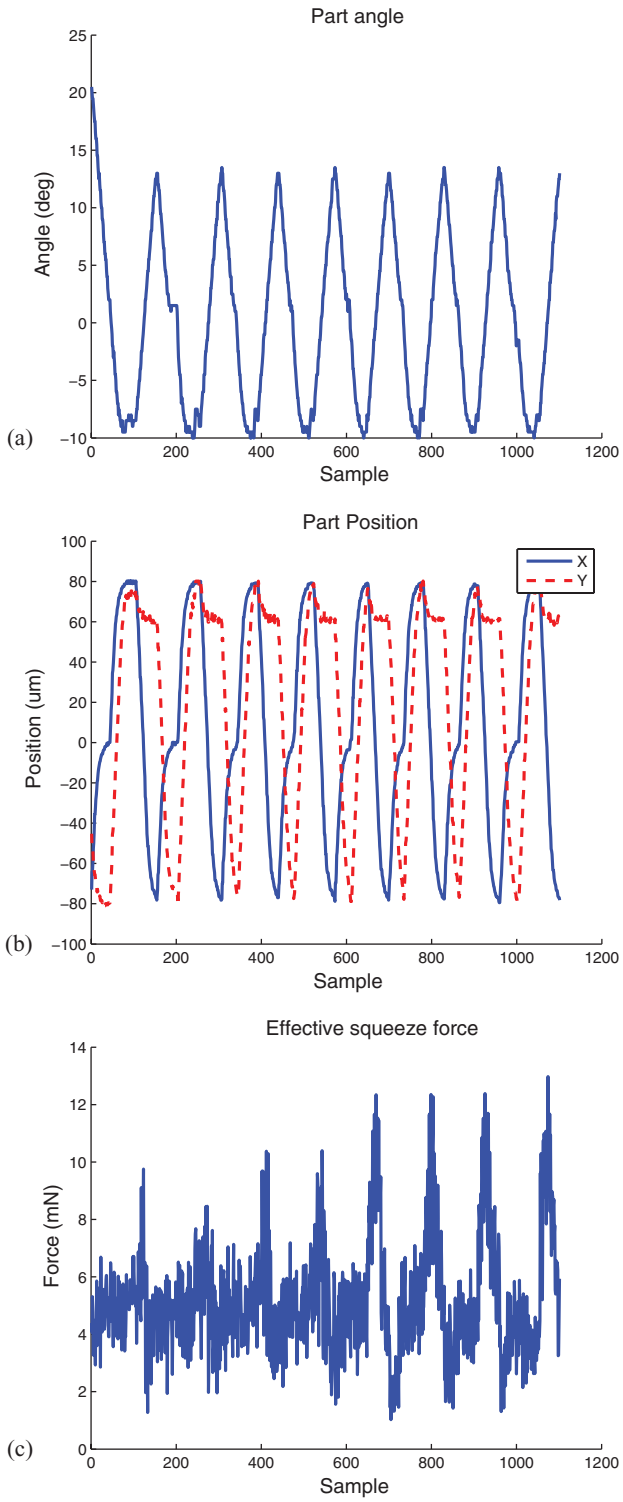

Fig. 18. Medium part executing a repeated motion sequence (a) angle (b) position (c) grip force versus sample.

C. Insertion Result

Using the motion and force control result together with pre-planned motion sequences, as described in Section II, we have demonstrated automated manipulation and insertion of a sub-millimeter part. Fig. 19 shows the part at different steps in the procedure. Fig. 19(a) shows the part at the beginning of the insertion procedure. Fig. 19(b) shows the part after being rotated. Fig. 19(c) shows the part after it has been grabbed by the probes using vision feedback. Fig. 19(d) and (e) shows the part at the start and the end of the out of plane rotation. The part is rotated past 90° to assist in sensing the bottom edge of the part with the top camera. Fig. 19(f) shows the part and slot after a sequence

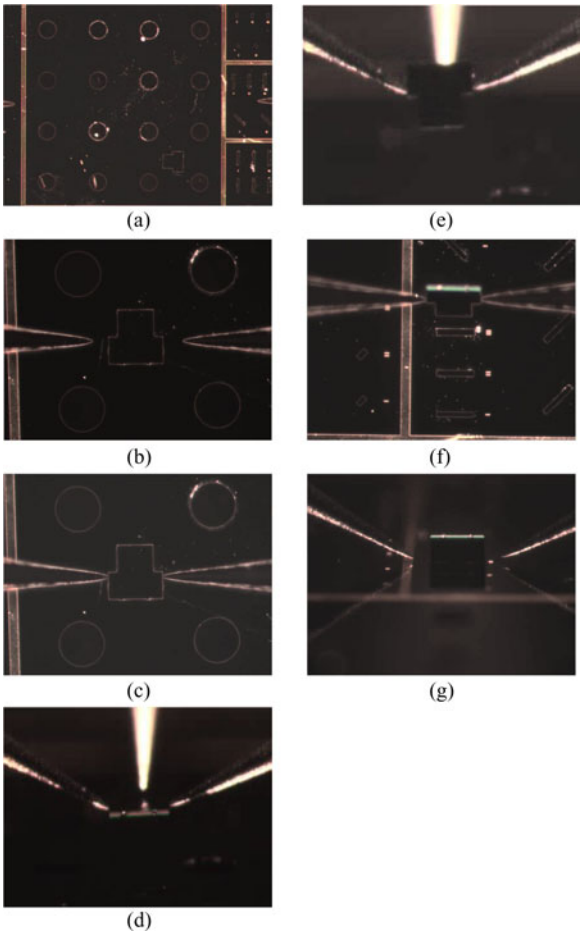

Fig. 19. (a) Initial part position. (b) Part rotated and probes moved close to part. (c) Probes gripping part after automated sequence. (d) Part at start of out of plane rotation. (e) Part after out of plane rotation. (f) Part and slot prealigned. (g) Part inserted.

that aligns the part. Finally, the part is inserted into the slot, as shown in Fig. 19(g).

The goal of this paper is to report our current proof-of-concept demonstration. For the planar case, the vision processing in terms of template matching and force estimation is very reliable. As a result, planar grasping and manipulation is very robust, with over 100 successful experiments conducted. The main failure mode of part grasping is due to contamination of the part (caused by the reuse of these parts for multiple experiments). It can typically be retried with little detrimental effects.

The 3-D automated assembly has been successfully demonstrated on five parts, but the insertion process is currently hampered by the difficulty to accurately measure the part orientation to align with the slot by using the existing camera configuration. With careful kinematic and vision calibration and large tolerance of the slot, successful insertion may be attained. The tolerances could be tightened with an additional camera to more accurately measure the part orientation during and after the rotation.

D. Experimental Force Calibration

Fig. 20 shows the results of an experimental measurement of the probe contact force versus the estimated force based on visual probe deflection. The experiment is conducted by pressing the probe against a piezoelectric force sensor, while simultaneously estimating the deflection using the visual force estimation shown in Section III-C. The force sensor is a Kronex AE801 sensor. The experiment verifies the accuracy of the visual force sensing. The confidence bounds are generated by considering the measurement error of the visual and piezoelectric force sensing. The error for piezoelectric measurement is caused by the calibration method. Proof masses of varying weight were hung off the end of the force sensor, and a linear fit was used to estimate the sensor parameters. The calibration experiment was done separately from the probe experiment. A separate chuck was used to hold the sensor, while proof masses were hung off the end. It is assumed that the position of the proof masses is within 0.5 mm of the end of the sensor. The other errors are insignificant compared with this error. The visual estimation error is caused mainly by the quantization of the pixels of the camera sensors. The confidence bound assumes that there is one pixel worth of error. There are some variations in the size of the confidence bound because of the method used to calculate the variation in pixel error and is an artifact of the analysis.

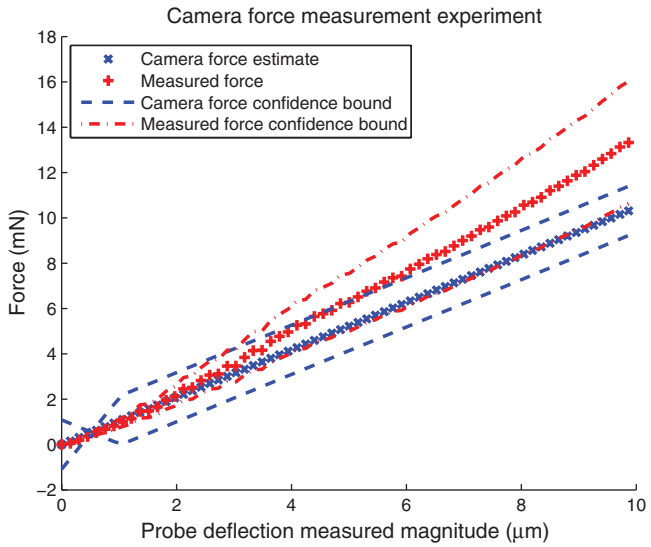

Fig. 20. Comparison of probe force measurement based on vision estimation and piezoelectric sensor.

Based on empirical evidence, it is estimated that the probe grasp force can vary between 2 and 15 mN and maintain a solid grasp.

VI. Conclusion

This paper has shown the feasibility of automated vision-guided microassembly using multiple coordinated probes. It provides an alternative to the conventional multitine microgripper approach and is particularly attractive for spatial (nonplanar) manipulation and handling of parts of widely varying sizes and geometry.

Current and future work focuses on the development of repeatable automatic sensing and manipulation of the part and the construction of more complex spatial mechanisms. This will

require the development of flexible software that can be rapidly adapted to different part geometries and assembly configurations. It will also require the ability to stack parts into structural elements. To assist in this development, a simulation software is being developed that will allow rapid trials of different concepts without investing large amounts of time and resources in physical experiments. The design and assembly technology will be applied to the development of active spatial microstructures: the foundation of future microrobotic applications.

ACKNOWLEDGMENT

The authors would like to thank Y. S. Kim for using finite-element models to calculate the stiffness of the various parts manipulated by the workstation probes. This work was performed in part at the National Institute of Standards and Technology Center for Nanoscale Science and Technology Nanofab.

REFERENCES

[1] D. Popa and H. Stephanou, "Micro and meso scale robotic assembly," *J. Manuf. Process*, vol. 6, no. 1, pp. 52–71, 2004.
[2] K. Petersen, "Silicon as a mechanical material," *Proc. IEEE*, vol. 70, no. 5, pp. 420–457, May 1982.
[3] G. Kovacs, N. Maluf, and K. Petersen, "Bulk micromachining of silicon," *Proc. IEEE*, vol. 86, no. 8, pp. 1536–1551, Aug. 1998.
[4] M. Savia and H. Koivo, "Contact micromanipulation—Survey of strategies," *IEEE/ASME Trans. Mechatronics*, vol. 14, no. 4, pp. 504–514, Aug. 2009.
[5] J. Fand and K. Böhringer, "Wafer-level packaging based on uniquely orienting self-assembly (the DUE-SPASS processes)," *J. Microelectromech. Syst.*, vol. 15, no. 3, pp. 531–540, 2006.
[6] R. Voyles and S. Hulst, "Micro/macro force-servoed gripper for precision photonics assembly and analysis," *Robotica*, vol. 23, no. 4, pp. 401–408, 2005.
[7] S. van Gastel, "Process requirements for high density SMD placement," Assembléon Netherlands B.V., Veldhoven, The Netherlands, Tech. Rep., 2009.
[8] F. Dionnet, D. Haliyo, and S. Régnier, "Autonomous micromanipulation using a new strategy of accurate release by rolling," in *Proc. IEEE Int. Conf. Robot. Autom.*, 2004, vol. 5, pp. 5019–5024.
[9] D. Popa, W. Lee, R. Murthy, A. Das, and H. Stephanou, "High yield automated MEMS assembly," in *Proc. IEEE Int. Conf. Autom. Sci. Eng.*, 2007, pp. 1099–1104.
[10] N. Sarkar, C. Baur, E. Stach, Z. Jandric, R. Stallcup, M. llis, G. Skidmore, J. Liu, and G. Fedder, "Modular MEMS experimental platform for transmission electron microscopy," in *Proc. IEEE Int. Conf. Microelectromech. Syst.*, 2006, pp. 146–149.
[11] N. Sarkar. (2005). Applying microassembly to real-world applications [Online]. Available: http://www.zyvex.com/Products/appnotes.html
[12] M. Last, V. Subramaniam, and K. Pister, "Out-of-plane motion of assembled microstructures using a single-mask SOI process," in *Proc. Int. Conf. Solid-State Sens., Actuators, Microsyst.*, 2005, vol. 1, pp. 684–687.
[13] C. Elbuken, M. B. Khamesee, and M. Yavuz, "Design and implementation of a micromanipulation system using a magnetically levitated MEMS robot," *IEEE/ASME Trans. Mechatronics*, vol. 14, no. 4, pp. 434–445, Aug. 2009.
[14] Y. Zhou and B. J. Nelson, "The effect of material properties and gripping force on micrograsping," in *Proc. IEEE Int. Conf. Robot. Autom.*, 2000, vol. 2, pp. 1115–1120.
[15] D. Popa, B. H. Kang, J. Wen, H. E. Stephanou, G. Skidmore, and A. Geisberger, "Dynamic modeling and input shaping of thermal bimorph MEMS actuators," in *Proc. IEEE Int. Conf. Robot. Autom.*, Sep. 2003, vol. 1, pp. 1470–1475.
[16] N. Dechev, L. Ren, W. Liu, W. Leghorn, and J. Millis, "Development of a 6 degree of freedom robotic micromanipulator for use in 3D MEMS microassembly," in *Proc. IEEE Int. Conf. Robot. Autom.*, 2006, pp. 281–288.
[17] N. Dechev, W. L. Cleghon, and J. K. Mills, "Microassembly of 3D microstructures using a compliant, passive microgripper," *J. Microelectromech. Syst.*, vol. 13, no. 2, pp. 176–189, 2004.
[18] J. Zhou, H. Chan, T. To, K. Lai, and W. Li, "Polymer MEMS actuators for underwater micromanipulation," *IEEE/ASME Trans. Mechatronics*, vol. 9, no. 2, pp. 334–342, Jun. 2004.
[19] F. Beyeler, A. Neild, S. Oberti, D. Bell, Y. Sun, J. Dual, and B. Nelson, "Monolithically fabricated microgripper with integrated force sensor for manipulating microobjects and biological cells aligned in an ultrasonic field," *J. Microelectromech. Syst.*, vol. 16, no. 1, pp. 7–15, 2007.
[20] R. Fearing, "Survey of sticking effects for micro parts handling," in *Proc. IEEE/RSJ Int. Conf. Intell. Robots Syst.*, 1995, vol. 2, pp. 212–217.
[21] Y. Zhang, B. Chen, X. Liu, and Y. Sun, "Autonomous robotic pick-and-place of microobjects," *IEEE Trans. Robot.*, vol. 26, no. 1, pp. 200–207, Feb. 2010.
[22] G. Yang, J. Gaines, and B. Nelson, "Optomechatronic design of microassembly systems for manufacturing hybrid microsystems," *IEEE Trans. Ind. Electron.*, vol. 52, no. 4, pp. 1013–1023, Aug. 2005.
[23] G. Yang, J. Gaines, and B. Nelson, "A supervisory wafer-level 3D microassembly system for hybrid MEMS fabrication," *J. Int. Robotic Syst.*, vol. 37, pp. 43–68, 2003.
[24] V. Vandaele, P. Lambert, and A. Delchambre, "Non-contact handling in microassembly: Acoustical levitation," *Precision Eng.*, vol. 29, no. 4, pp. 491–505, 2005.
[25] K. Bohringer, K. Goldberg, M. Cohn, R. Howe, and A. Pisano, "Parallel microassembly with electrostatic force fields," in *Proc. IEEE Int. Conf. Robot. Autom.*, 1998, vol. 2, pp. 1204–1211.
[26] T. Tanikawa and T. Arai, "Development of a micro-manipulation system having a two-fingered micro-hand," *IEEE Trans. Robot. Autom.*, vol. 15, no. 1, pp. 152–162, Feb. 1999.
[27] C. Keller and R. Howe, "Hexsil tweezers for teleoperated microassembly," in *Proc. IEEE. 10th Annu. Int. Workshop Micro Electro Mechanical Syst.*, 1997, pp. 72–77.
[28] J. Thompson and R. Fearing, "Automating microassembly with orthotweezers and force sensing," in *Proc. IEEE/RSJ Int. Conf. Intell. Robots Syst.*, 2001, vol. 3, pp. 1327–1334.
[29] W. Zesch and R. S. Fearing, "Alignment of microparts using force controlled pushing," in *Proc. SPIE Conf. Microrobot. Microassembly*, 1998, vol. 3834, pp. 195–202.
[30] M. Moll, K. Goldberg, M. Erdmann, and R. Fearing, "Orienting microscale parts with squeeze and roll primitives," in *Proc. IEEE Int. Conf. Robot. Autom.*, 2002, vol. 2, pp. 1931–1936.
[31] P. Cheng, B. Gavrea, and V. Kumar, "Planning and control of meso-scale manipulation tasks with uncertainties," presented at the Robot.: Sci., Syst. Conf., Atlanta, GA, 2007.
[32] D. Cappelleri, P. Cheng, J. Fink, B. Gavrea, and V. Kumar, "Automated assembly for mesoscale parts," *IEEE Trans. Robot. Autom.*, vol. 8, no. 3, pp. 598–613, Jul. 2011.
[33] E. Shimada, J. Thompson, J. Yan, R. Wood, and R. Fearing, "Prototyping millirobots using dextrous microassembly and folding," presented at the ASME Symp. Microrobotics, Orlando, FL, 2000.
[34] A. Ferreira, C. Cassier, and S. Hirai, "Automatic microassembly system assisted by vision servoing and virtual reality," *IEEE/ASME Trans. Mechatronics*, vol. 9, no. 2, pp. 321–333, Jun. 2004.
[35] J. J. Gorman and N. G. Dagalakis, "Probe-based micro-scale manipulation and assembly using force feedback," in *Proc. Int. Conf. Robot. Remote Syst. Hazardous Environ.*, 2006, pp. 621–628.
[36] K. Rabenorosoa and C. Clévy, P. Lutz, "Active force control for robotic micro-assembly: Application to guiding tasks," in *Proc. IEEE Int. Conf. Robot. Autom.*, May 2010, pp. 2137–2142.
[37] J. Wason, J. Wen, Y. Choi, J. Gorman, and N. Dagalakis, "Vision guided multi-probe assembly of 3D microstructures," in *Proc. IEEE/RSJ Int. Conf. Intell. Robots Syst.*, Oct. 2010, pp. 5603–5609.
[38] J. Wen and L. Wilfinger, "Kinematic manipulability of general constrained rigid multibody systems," *IEEE Trans. Robot. Autom.*, vol. 15, no. 3, pp. 558–567, Jun 1999.
[39] J. D. Wason, W. T. Gressick, J. T.-Y. Wen, J. J. Gorman, and N. G. Dagalakis, "Multi-probe micro-assembly," in *Proc. IEEE Conf. Autom. Sci. Eng.*, Sep. 2007, pp. 63–68.
[40] L. Wilfinger, J. Wen, and S. Murphy, "Integral force control with robustness enhancement," *IEEE Control Syst. Mag.*, vol. 14, no. 1, pp. 31–40, Feb. 1994.
[41] L. Meirovitch, *Analytic Methods in Vibration*. New York: MacMillan, 1967.

[42] R. Bowling, "A theoretical review of particle adhesion," in *Particles on Surfaces1: Detection, Adhesion and Removal*, K. Mittal, Ed. New York: Plenum, 1988, pp. 129–155.
[43] J. Collins, *Mechanical Design of Machine Elements and Machines*. Hoboken, NJ: Wiley, 2003.
[44] D. B. Asay and S. H. Kim, "Effects of adsorbed water layer structure on adhesion force of silicon oxide nanoasperity contact in humid ambient," *J. Chem. Phys.*, vol. 124, p. 174712, 2006.
[45] K. Yesin and B. Nelson, "Robust CAD model based visual tracking for 3D microassembly using image space potentials," in *Proc. IEEE Int. Conf. Robot. Autom.*, 2004, vol. 2, pp. 1868–1873.
[46] R. Haralick and L. Shapiro, *Computer and Robot Vision*. vol. 1, Reading, MA: Addison-Wesley, 1992.
[47] R. Gonzalez, R. Woods, and S. Eddins, *Digital Image Processing using Matlab*. Upper Saddle River, NJ: Prentice–Hall, 2004.
[48] J. D. Wason, "Visually-guided multi-probe microassembly of spatial microelectromechanical systems," Ph.D. dissertation, Rensselaer Polytech. Inst., Troy, NY, Dec. 2011.

John D. Wason (M'12) received the B.S. degree in 2006, the M.S. degree in 2007, and Ph.D. degree from Rensselaer Polytechnic Institute (RPI), Troy, NY. He was an Intern with the Jet Propulsion Laboratory, Pasadena, CA, while an undergraduate with RPI.

He is currently a Research Engineer with the Center for Automation Technologies and Systems (CATS), RPI. He joined CATS as a Graduate Research Assistant in 2006 and joined the staff after receiving the Ph.D. degree in 2011. His research interests include robotics, mechatronics, embedded systems, and microtechnology.

John T. Wen (F'01) received the B.Eng. degree from McGill University, Montreal, QC, Canada, in 1979, the M.S. degree from University of Illinois, Chicago, in 1981, and the Ph.D. degree from Rensselaer Polytechnic Institute, Troy, NY, in 1985, all in electrical engineering.

From 1981 to 1982, he was a System Engineer with Fisher Controls, developing a plant-wide coordination control system for pulp and paper plants. From 1985 to 1988, he was a member of technical staff with the Jet Propulsion Laboratory, Pasadena, CA, working on modeling and control algorithm development for large space structures and space robots. Since 1988, he has been with Rensselaer Polytechnic Institute, where he is currently a Professor with the Department of Electrical, Computer, and Systems Engineering with a joint appointment with the Department of Mechanical, Aerospace, and Nuclear Engineering. He is also the Director of a New York State Center for Advanced Technology, Center for Automation Technologies and Systems. His research interest lies in the general area of dynamical systems modeling and control with applications to vibration suppression, robot manipulation, opto-mechatronics systems, thermal management, and flow control.

Dr. Wen was an American Society for Engineering Education/National Aeronautics and Space Administration Summer Faculty Fellow in 1993 and a Japan Society for the Promotion of Science Senior Visiting Scientist in 1997. He was selected as an Oversea Assessor by the Chinese Academy of Sciences in 2004.

Jason J. Gorman received the B.S. degree in aerospace engineering from Boston University, Boston, MA, in 1994 and the M.S. and Ph.D. degrees in mechanical engineering from the Pennsylvania State University, University Park, in 1999 and 2002, respectively.

He joined the National Institute of Standards and Technology, Gaithersburg, MD, in 2002 as a National Regulatory Commission Postdoctoral Research Associate, and since then, he has been a member of the technical staff with the Intelligent Systems Division. His research interests include micro- and nanoelectromechanical systems, scanning probe microscopy, nanomanufacturing, precision measurements, dynamic systems, and robust and nonlinear control.

Nicholas G. Dagalakis (SM'10–LSM'12) received the M.S., Eng.D., and Ph.D. degrees from the Massachusetts Institute of Technology (MIT), Cambridge, and the Diploma degree in mechanical and electrical engineering from the National Technical University of Greece, Athens, Greece.

He has worked for MIT as a Research Associate and the University of Maryland, College Park, as an Assistant Professor. He joined the National Institute of standards and Technology (NIST), Gaithersburg, MD, in 1985 as a full-time Research Staff. He has conducted research in electrical generation, biomedical engineering, robotics, high-precision micro/nano manufacturing, sensors, and standards. Since 1999, he has been a Project Leader on several NIST and other agency funded projects. He has contributed to 25 journals and 52 conference publications and has coauthored four reports, two books, and two patents.

Dr. Dagalakis received a U.S. Senate Special Committee on Aging Award in 2008 and an NIST Bronze Medal Award in 2009.